ORIGINAL PAPER

AC impedance analysis, equivalent circuit, and modulus behavior of NaFeP$_2$O$_7$ ceramic

S. Nasri · M. Megdiche · M. Gargouri

Abstract II-NaFeP$_2$O$_7$ was prepared by conventional ceramic fabrication technique. Rietveld refinement, impedance properties, conductivity dispersion, electric modulus, and their scaling were carried out as a function of frequency and temperature. Thus, X-ray diffraction analysis indicates that the sample exhibits a single-phase nature with a monoclinic structure. In addition, analysis of Nyquist plots as well as modulus analysis revealed the contribution of two electrically active regions corresponding to bulk mechanism and distribution of grain boundaries. The near values of activation energies, obtained from the impedance and modulus spectra, confirm that the transport happens through an ion hopping mechanism, dominated by the motion of the Na$^+$ ions in the framework of the investigated material resulting from intersecting tunnels or voids where Na$^+$ is located.

Introduction

The metal diphosphates A^{I}M^{III}P$_2$O$_7$ show a variety of structure types that are controlled by the stereochemical behaviors of the A and M cations. On the one hand, they affect the coordination numbers, the degree of distortion of the coordination polyhedra, and the conformation of the P$_2$O$_7$ groups.

S. Nasri (✉) · M. Megdiche · M. Gargouri
Condensed Matter Laboratory, Faculty of Sciences, University of Sfax, B.P. 1171, 3000 Sfax, Tunisia
e-mail: nasri.saber.1@gmail.com

M. Megdiche
e-mail: megdichemegdiche@gmail.com

Research focus, on the development of such materials, is on the rise. On the other hand, these materials, in particular for M=Fe with all the alkali cations, are fascinating as they comprise electrically and/or magnetically active transition metal ions [1]. Such a significant class of materials is widely used in the making of transformers, chokes, microwave absorbers, and sensors [2–4]. Besides, recently, some of them have been proposed as cathode materials for lithium batteries [5–8] and even as nanoparticles for decontamination and remediation of water [9].

Among these compounds, NaFeP$_2$O$_7$ is an interesting candidate, mainly due to its prospective potential technological applications. This latter presents two structures [10]: a low temperature form, called NaFeP$_2$O$_7$-I [11, 12], and a high-temperature form, known as NaFeP$_2$O$_7$-II [11–13].

Recently, we have reported the electrical properties of the KFeP$_2$O$_7$ and AgFeP$_2$O$_7$ compounds [14, 15], and as continuity, we have synthesized the II-NaFeP$_2$O$_7$. Hence, the purpose of the present work is to determine the equivalent electrical circuit which can model the experimental data and characterize the electrical microstructure via impedance spectroscopy in a wide range of frequencies and temperatures.

Experimental

For the sake of an easy and satisfying understanding of the topic of this paper, an explanation of the characteristics and fabrication of the sample as well as the description of the details related to the way measurements are performed is given here.

The II-NaFeP$_2$O$_7$ ceramic sample was prepared by a standard high-temperature solid-state reaction technique using AR grade (purity more than 99.5 %, Hi-Media) oxides and/or carbonates: Na$_2$CO$_3$, Fe$_2$O$_3$, and NH$_4$H$_2$PO$_4$ in a suitable stoichiometry. The abovementioned

Fig. 1 Powder X-ray diffraction pattern and Rietveld refinement for the sample II-NaFeP$_2$O$_7$
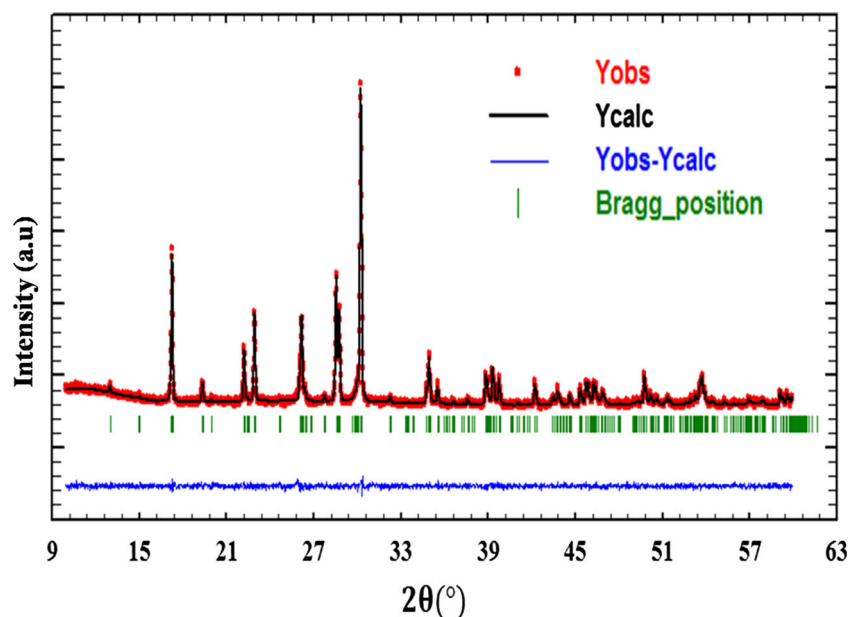
ingredients were mixed thoroughly in air using an agate mortar and pestle. This mixture was calcined at an optimized temperature of 573 K for about 8 h in an open silica crucible air using an electrical furnace to eliminate NH_3, CO_2, and H_2O. Then, the calcined powder of circular disc-shaped pellets was fabricated by applying a uniaxial pressure of 3 T/cm^2. Once again, the pellets were subsequently sintered at an optimized temperature of 1,073 K in air atmosphere for about 8 h.

Characterization of the compound has been carried out by powder X-ray diffraction (XRD). Thereby, the XRD pattern of the material was recorded at room temperature using a Philips powder diffractometer PW 1710 with CuKα radiation (λ=1.5405 Å) in a wide range of Bragg angles ($9° \leq 2\theta \leq 63°$).

The dielectric property and conductivity (AC–DC) measurements of the sample were made by a Tegam 3550 ALF impedance analyzer by sandwiching circular pellets of a diameter 8 mm and a thickness of about 1 mm thickness between platinum electrodes. Measurements were carried out at temperatures from 573 to 700 K (frequency range 209 Hz to 5 MHz). Specifically, the temperature of the sample was measured with the aid of a copper-constantan thermocouple placed near the sample.

Results and discussions

Crystalline parameters

The X-ray diffraction study of the sample was carried out at room temperature and the data were analyzed with the Rietveld refinement technique using the FullProf code. Figure 1 shows the XRD spectrum of II-NaFeP$_2$O$_7$ powder at room temperature. The quality factors are R_B=3.15, R_F=4.26, and χ^2=1.29 indicating a good agreement between the observed and calculated profiles and no trace of any extra peaks was found, thereby suggesting the formation of a single-phase compound having the monoclinic P21$_{/C}$ space group with lattice parameters a=7.325 (3) Å, b=7.903 (4) Å, c=9.574 (4) Å, β=111.819 (9)°, and V=514.622 (7) Å^3. These parameters are very similar to those previously published for the II-NaFeP$_2$O$_7$ compound [16].

At this point, the structure of the diphosphate II-NaFeP$_2$O$_7$ is known and it is isostructural with AgFeP$_2$O$_7$ [17]. In fact, it can be described as a cage structure whose host lattice FeP$_2$O$_7$ is built up from corner-sharing octahedra and P$_2$O$_7$ groups. The pyro group is formed from two slightly distorted PO$_4$ groups having one common oxygen. Each PO$_4$ tetrahedron shares its corners with three octahedra and one tetrahedron, while a FeO$_6$ octahedron shares all its apices with PO$_4$ tetrahedra. Additionally, all the P$_2$O$_7$ groups have a lengthening direction parallel to a. The arrangement of the polyhedral allows us to distinguish two sorts of layers parallel to (001): the octahedral layers with the composition FeO$_3$ and the tetrahedral layers with the composition P$_2$O$_4$. These layers are alternately stacked along c in such a way that every P$_2$O$_7$ group shares four corners with one octahedral layer, and the two other corners with the other octahedral layer. Two sorts of tunnels are indeed observed as very wide tunnels running along the [001] direction and distorted hexagonal tunnels running along the [110] direction which could be able to exhibit mobility of the inserted Na$^+$ [14].

Fig. 2 **a**, **b** Complex impedance spectrum as a function of temperature with electrical equivalent circuit (*inset*), accompanied by theoretical data calculated with expressions (2) and (3)
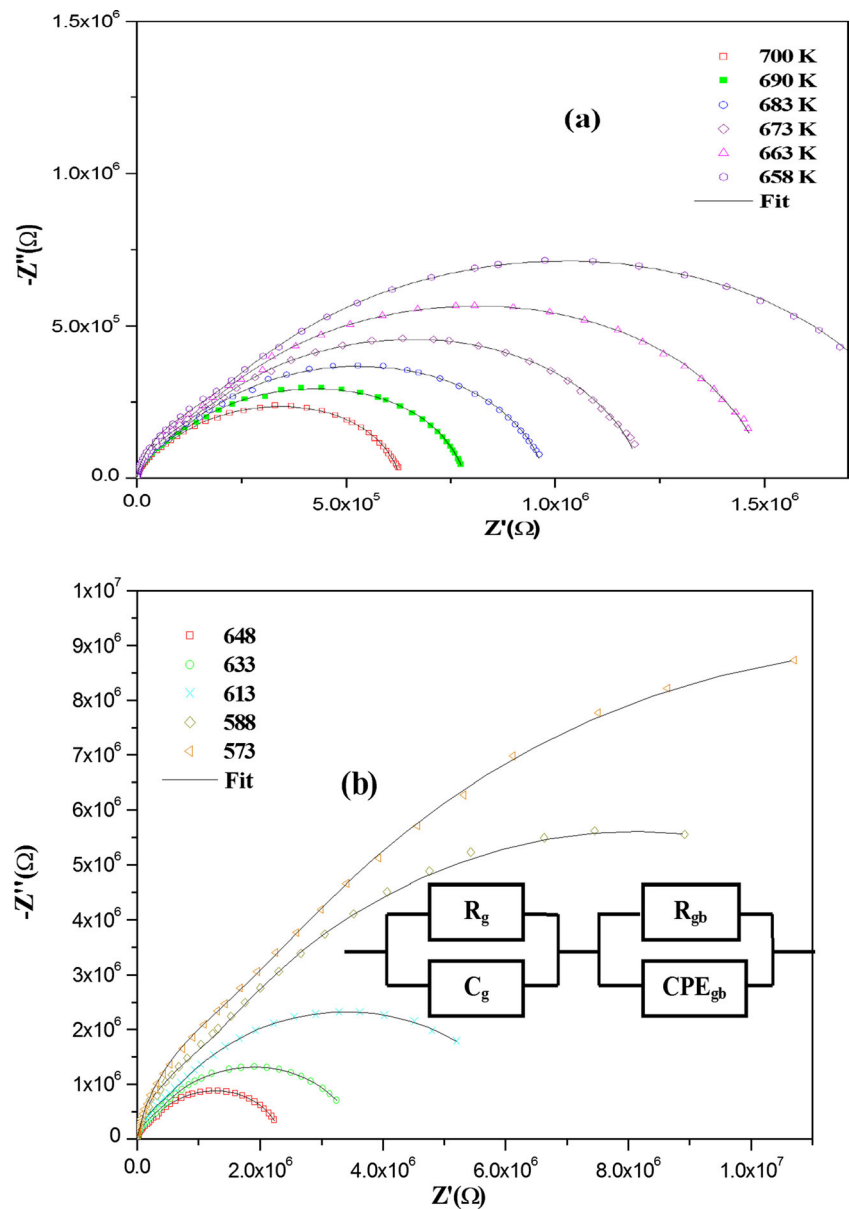

Impedance analysis

The complex impedance spectroscopy is an important tool to analyze the electrical properties and to get more information about the relaxation process of the investigated device [18]. This technique shows the response of a sample to a sinusoidal perturbation and gives the impedance as a function of frequency. The resultant response (when plotted in a complex plane which is known as Nyquist diagrams) appears in the form of a succession of semicircles representing electrical phenomena inside the material due to the bulk, grain boundary, and interface. In this plot, we expect a separation of the bulk phenomena from the surface (grain boundary) phenomena

[19]. In fact, evaluation of the real and imaginary impedance curves is preferred in terms of equivalent circuit representation of the sample and evaluation of any relaxation mechanism, in case of its existence. To study the contribution due to different effects, the impedance plane plots have been performed at different temperatures in the frequency range of 209 Hz–5 MHz.

Characteristically, two semicircular arcs have been observed (Fig. 2a, b). In order to study and understand the impedance spectrum, it is helpful to have an equivalent circuit model that provides a sensible illustration of the electrical properties of the observed regions. As a matter of fact, the high-frequency semicircle is due to the grain and the one at

Fig. 3 a, b The real and the imaginary parts of the impedance as a function of angular frequency at several temperatures
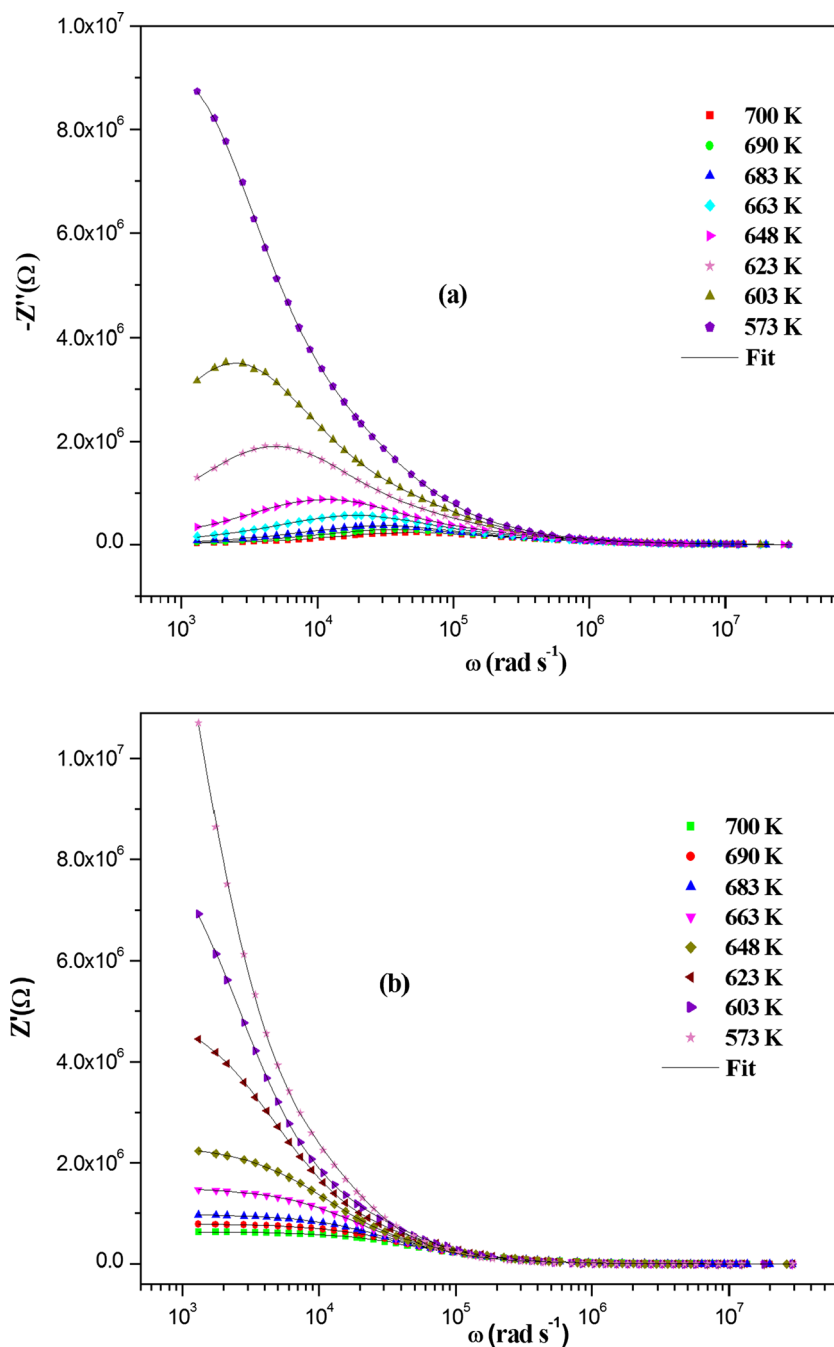
lower frequencies, which exhibits some degree of depression instead of a semicircle centered on the abscissa axis assigned to the grain boundary [18, 20]. Thus, a typical equivalent circuit consisting of a series of combinations of grains and grain boundary elements was thereby used to fit the measured data. The first consists of a parallel combination of resistance (R_g) and capacitance (C_g), whereas the second consists of a parallel combination of resistance (R_{gb}) and a constant phase element CPE_{gb}.

The impedance of CPE_{gb} is given by:

$$Z_{CPE_{gb}} = \frac{1}{\left[Q_{gb}(i\omega)^{\alpha}\right]} \tag{1}$$

where Q_{gb} indicates the value of the capacitance of the CPE_{gb} element and α represents the magnitude of the

departure of the electrical response from an ideal condition and also indicates the degree of depression of arc below the real axis.

In the present situation, the real and imaginary components of the whole impedance were calculated according to the following expressions:

$$Z' = \frac{R_g}{1 + (\omega R_g C_g)^2}$$

$$+ \frac{R_g^2 Q_{gb} \omega^{\alpha_{gb}} \cos\left(\frac{\alpha_{gb}\pi}{2}\right) + R_{gb}}{\left(1 + R_g Q_{gb} \omega^{\alpha_{gb}} \cos\left(\frac{\alpha_{gb}\pi}{2}\right)\right)^2 + \left(R_g Q_{gb} \omega^{\alpha_{gb}} \sin\left(\left(\frac{\alpha_{gb}\pi}{2}\right)\right)\right)^2}$$

$$(2)$$

$$Z'' = R_g \left[\frac{\omega R_g C_g}{1 + (\omega R_g C_g)^2}\right]$$

$$+ \frac{R_g^2 Q_{gb} \omega^{\alpha_{gb}} \sin\left(\frac{\alpha_{gb}\pi}{2}\right)}{\left(1 + R_g Q_{gb} \omega^{\alpha_{gb}} \cos\left(\frac{\alpha_{gb}\pi}{2}\right)\right)^2 + \left(R_g Q_{gb} \omega^{\alpha_{gb}} \sin\left(\left(\frac{\alpha_{gb}\pi}{2}\right)\right)\right)^2}$$

$$(3)$$

Figure 3a, b shows the experimental and calculated values of real and imaginary parts of the impedance (Z' and Z'') as a function of frequency at different temperatures (573–700 K) using the equivalent circuit. Typical curves are observed in the previously mentioned figures. The temperature affects strongly the magnitude of resistance. At lower temperatures, Z' decreases monotonically with increases in frequency up to a certain frequency and then becomes frequency independent (Fig. 3a). Moreover, the magnitude of Z'' maxima decreases with temperatures showing the thermally activated nature of the relaxation time as well as an increasing loss in resistive property of the sample. This behavior of the impedance pattern arises possibly due to the presence of space charge in the materials [21].

Figure 4 shows the frequency dependence of Z' and Z'' fits to the equivalent circuit and their corresponding Argand diagram [22, 23] (inset figure) drawn at 690 K in II-NaFeP$_2$O$_7$. It is clear that Z'' increases, whereas Z' decreases, and at a particular frequency, Z'' occupies a maximum value and Z' intersects, and above this frequency, both values merge with the X-axis. Those diagrams clearly show a good agreement between theoretical and experimental data. The extracted parameters, as obtained from the ZView software, are collected

in Table 1. The capacitance values of the high- and the low-frequency semicircles are found to be in the range of 10^{-12} and 10^{-10} F, respectively, proving that the observed semicircles represent the bulk and grain boundary response of the system, respectively [24, 25].

Thus, the obtained values of bulk resistance (R_g), corresponding to the grain at different temperatures, enable finding the electrical conductivity σ_g defined by the relation as follows:

$$\sigma_g = \frac{e}{R_g * s} \qquad (4)$$

where $\frac{e}{s}$ represents the sample geometrical ratio.

The temperature dependence of the conductivity $\sigma_{g,gb}$ of II-NaFeP$_2$O$_7$ is represented in Fig. 5 in the form of $Ln(\sigma_{g,gb} T)$ vs. $1,000 / T$. An Arrhenius type behavior $\sigma_{g,gb} T = \sigma_0 \exp(-E_a / k_B T)$ is shown. While E_a is the activation energy, T is the absolute temperature, k_B is Boltzmann's constant, and σ_0 is the pre-exponential factor which includes the charge carrier mobility and density of states.

Both σ_g (grain) and σ_{gb} (grain boundary) increase with increasing temperature, indicating that the electrical conduction in the material is a thermally activated process. For the whole studied temperature ranges, the bulk conductivity is higher than the grain boundary one. The value of activation energy estimated from the Arrhenius plot of σ_g and σ_{gb} with respect to $1,000 / T$ is 0.85 (2) eV and 0.83 (3) eV, respectively. Thus, we notice that the bulk and the grain boundary activation energy values are very close. This indicates that the conduction of the grain and the grain boundary increases at a similar rate with an increase in temperature.

Electric modulus analysis

Electrical transport process parameters (such as carrier/ion hopping rate, conductivity relaxation time, etc.) in ceramic materials can be analyzed via complex electric modulus formalism. Although the physical meaning of this type of representation is still controversially discussed, the dielectric modulus is frequently used in the analysis of dielectric data of ionic conductors [26].

The electric modulus $M^*(\omega)$ as expressed in the complex modulus formalism is:

$$M^*(\omega) = M' + iM''$$

where $M' = \omega C_0 Z''$, $M'' = \omega C_0 Z'$, and C_0 is the vacuum capacitance of the cell. The graph of the imaginary part of the dielectric modulus, as a function of frequency at different

Fig. 4 Variation of Z' and Z'' with angular frequency at 690 K; *inset* is the Cole–Cole plot at the same temperature
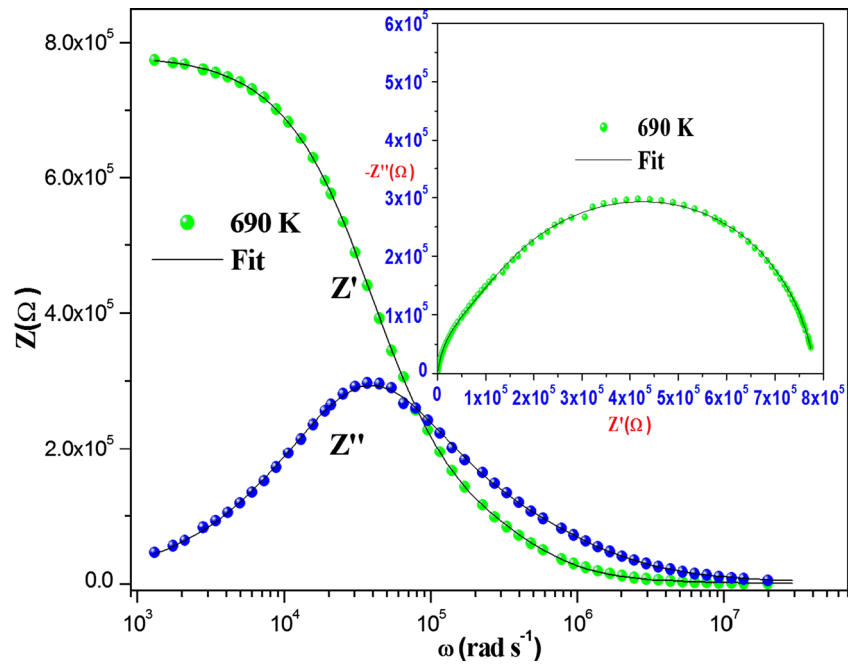
temperatures, is shown in Fig. 6. As a matter of fact, two relaxation peaks are observed in the patterns. Thus, the smaller peak at the lower frequency is associated with the grain boundary effect, and the well-defined one at the higher frequency is correlated with the bulk effects. The positions of these relaxation peaks are found to shift to higher frequencies with the increase of the temperature showing a temperature-dependent relaxation, as well as a correlation between motions of mobile ion charges [27]. From the view of the higher frequency peak of M'' for each temperature, the frequency region below the peak represents the range in which the charge carriers are mobile over long distances [28], whereas the frequency region above the peak determines the range in which the charge carriers are confined to the potential wells being mobile on short distances within the wells [29, 30].

A conventional equation to fit the frequency dependence curve of M'', at constant temperature, in a variety of materials, is based on the Havriliak–Negami equation [31]. In this case, the electric modulus is given by:

$$M^* = M_\infty[1 - \varphi_{HN}(\omega)] = M_\infty\left[1 - \frac{1}{[1 + (i\omega\tau)^\alpha]^\gamma}\right] \quad (5)$$

HN is the Havriliak–Negami (HN) function and both HN parameters α and γ define the Kohlrausch parameter β as $\beta = (\alpha\gamma)^{1/1.23}$. Therefore, in order to simulate the two relaxation peaks, we have modified the above expression as follows:

$$M^* = M_\infty\left[1 - \frac{1}{\left[1 + (i\omega\tau_g)^{\alpha_g}\right]^{\gamma_g}}\right] \quad (6)$$

$$+ M_S\left[1 - \frac{1}{\left[1 + (i\omega\tau_{gb})^{\alpha_{gb}}\right]^{\gamma_{gb}}}\right]$$

where $M_\infty = 1 / \varepsilon_\infty$, $M_S = 1 / \varepsilon_S$, ε_∞, and ε_S being the high- and low-frequency asymptotic values of the real part of the

Table 1 The equivalent circuit parameters for the NaFeP$_2$O$_7$ sample

T (K)	R_g (KΩ)	C_g (10^{-12} F)	R_{gb} (KΩ)	Q_{gb} (10^{-10} F)	α_{gb}
573	1,412.20	2.21	19,014	0.79	0.90
588	925.76	2.25	12,730	0.90	0.899
603	610.35	2.28	8,298.30	1.04	0.880
613	410.82	2.38	5,654.20	1.17	0.872
623	345.01	24	4,665.20	1.22	0.870
633	236.75	25	3,254.40	1.30	0.865
643	195.76	2.54	2,693.70	1.38	0.862
648	159.87	2.58	2,183.50	1.45	0.859
658	133.26	2.64	1,770.40	1.48	0.858
663	108.64	2.68	1,405	1.51	0.857
673	87.546	2.78	1,133.30	1.57	0.855
683	72.064	2.87	913.85	1.60	0.854
690	58.791	2.97	732.58	1.63	0.853
700	47.346	3.12	586.93	1.64	0.852

Fig. 5 σ_g and σ_{gb} as a function of temperature
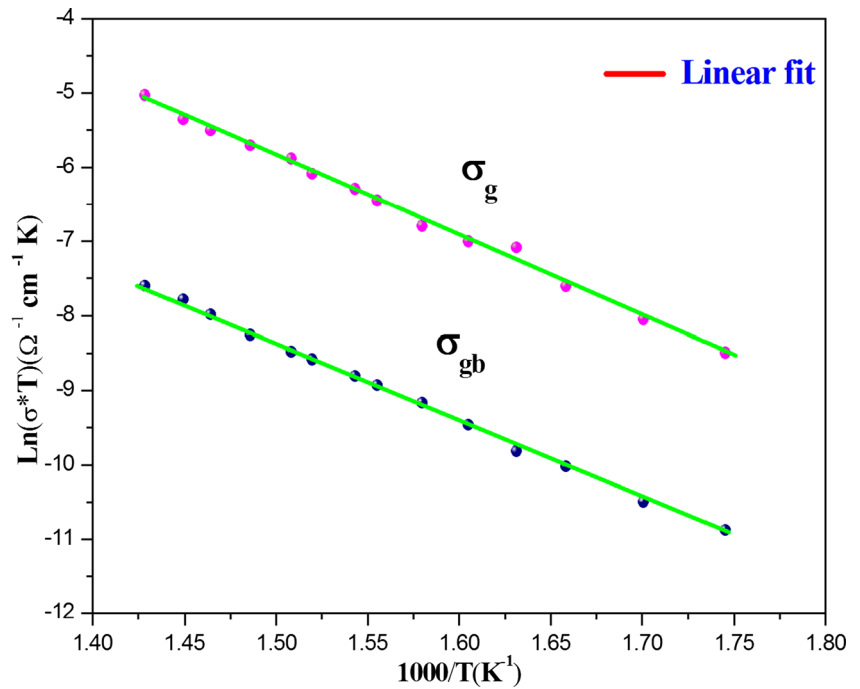
dielectric permittivity, respectively. The parameters α_g and γ_g represent the shape of the high-frequency peak corresponding to the grains, and α_{gb} and γ_{gb} are the corresponding quantities for the low-frequency peak [19]. A good fit was performed using this equation as shown in Fig. 6.

The high-frequency peak in the M'' curves is found to be asymmetric, implying a nonexponential behavior of the bulk conductivity relaxation. This type of behavior suggests the

possibility that the ion migration takes place via hopping accompanied by a consequential time-dependent mobility of other charge carriers of the same type in their vicinity [32, 33]. The nonexponential conductivity relaxation is well described by a Kohlrausch–Williams–Watts (KWW) function [34]:

$$\varphi(t) = \exp\left[\left(\frac{-t}{\tau}\right)^{\beta}\right] \qquad 0 < \beta < 1 \qquad (7)$$

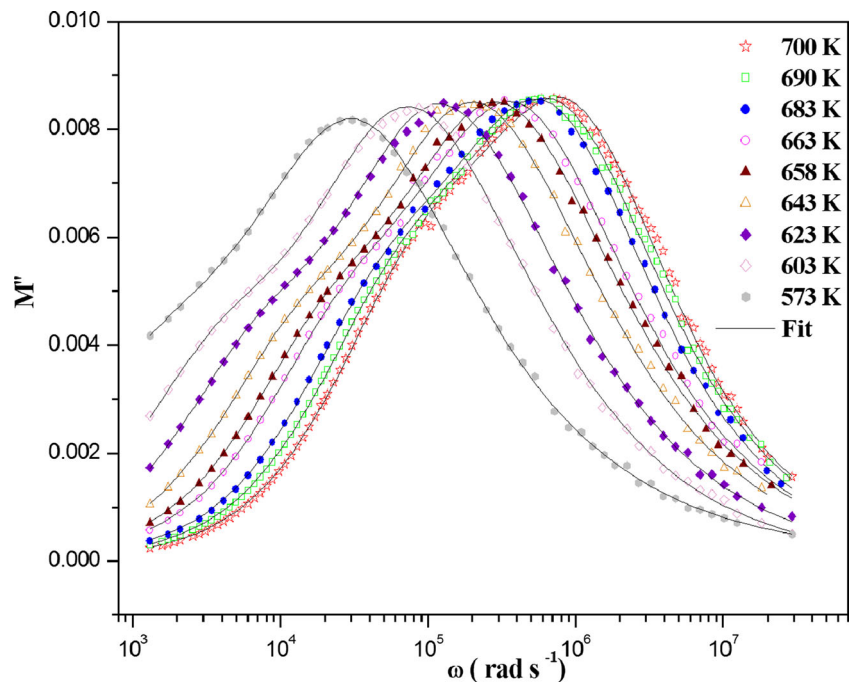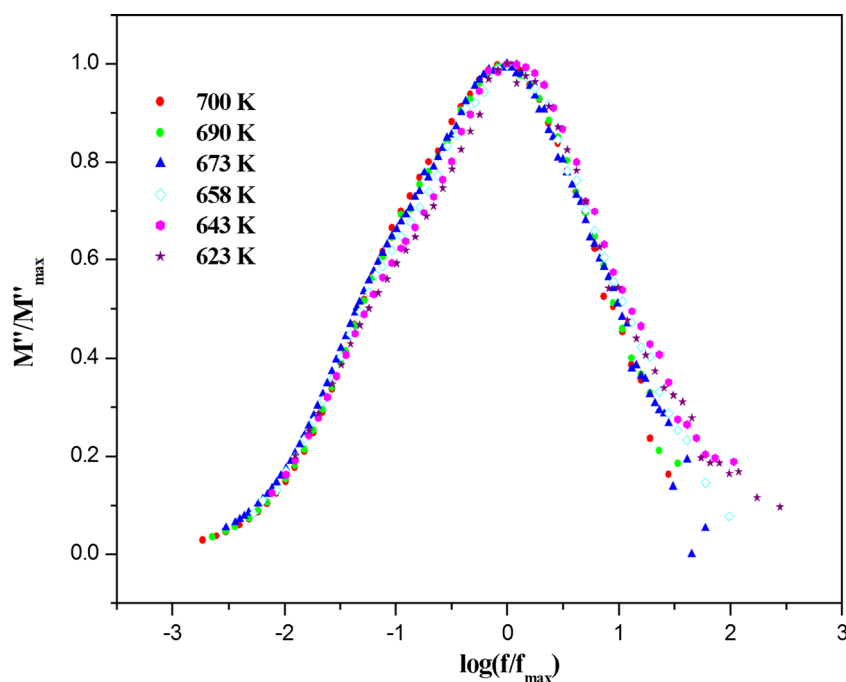**Fig. 6** Frequency dependence of the imaginary part of the electric modulus at several temperatures

Fig. 7 Normalized plots of M'' / M''_{max} vs. $Ln(f / f_{max})$ for II-NaFeP$_2$O$_7$ at different temperatures

where $\varphi(t)$ represents the distribution of relaxation time in ion-conducting materials and τ is the conductivity relaxation time. The value of β determined from the full width at half maximum (FWHM) of the high-frequency peak (β=1.14/FWHM) and the β obtained by fitting the M'' curve to Eq. 6 are very close. Therefore, the β values obtained lie in the range of 0.72 for the high-frequency peak, whereas for the peak at low frequency, it is found to be between 0.61 and 0.68. Hence, the variations of the relaxation frequency with temperature for the bulk and the grain boundary follow the Arrhenius behavior, as shown in Fig. 5. The activation energy calculation was based on the slopes of the Log ($\omega_{g,gb}$) vs. 1,000 / T plot. Consequently, the activation energy values are E_g=0.84 (3) eV and E_{gb}=0.83 (4) eV. In short, the spectra are close enough to suggest that the Na$^+$ ion transport is probably due to a hopping mechanism through tunnels presented in the structure of II-NaFeP$_2$O$_7$. Otherwise, these values are typical values for ionic conduction mechanism [35, 36].

Figure 7 shows the M'' / M''_{max} vs. Log (f / f_{max}) at different temperature (normalized plot), and it shows the scaling behavior in the material. This is called the modulus master curve that enables us to have an insight into the dielectric processes occurring in the material. It is characterized by a broad asymmetric pattern with a crossover from the long range. Moreover, it shows that the shape and FWHM of the asymmetric M'' / M''_{max} curve remain constant in the temperature range studied, implying a nonexponential behavior of the conductivity relaxation. Indeed, the approximate overlap of the modulus curves for all temperatures indicates the dynamical processes occurring at different frequencies and independence of temperature. This has usually been regarded as an indication of a distribution of relaxation times in the conduction process occurring in the material. Consequently, this might be due to the ion migration that takes place via the hopping mechanism [37].

Frequency and temperature dependence of AC conductivity

The conductivity spectra throw light on the hopping motion of the mobile ions. Hence, a typical frequency dependence of AC conductivity within the considered temperature ranges for the sample is shown in Fig. 8. As a matter of fact, the values of the AC conductivity were calculated from the complex impedance data using:

$$\sigma_{AC} = \left(\frac{e}{s}\right)\left(\frac{Z'}{Z'^2 + Z''^2}\right) \tag{8}$$

where Z' and Z'' are the real and the imaginary parts of the complex impedance, and e and s are the thickness and the area, respectively, of the present pellet.

The frequency-dependent conductivity spectrum shows a low-frequency plateau, followed by a region that is sensitive to frequency as well as temperature. The frequency-independent region characterizes the DC conductivity due to the random diffusion of the ionic charge carriers via activated hopping. However, for the region of frequencies where conductivity increases markedly with

Fig. 8 Variation of AC conductivity of II-NaFeP$_2$O$_7$ with frequency and temperature. The *solid lines* are the best fits to Eq. 8
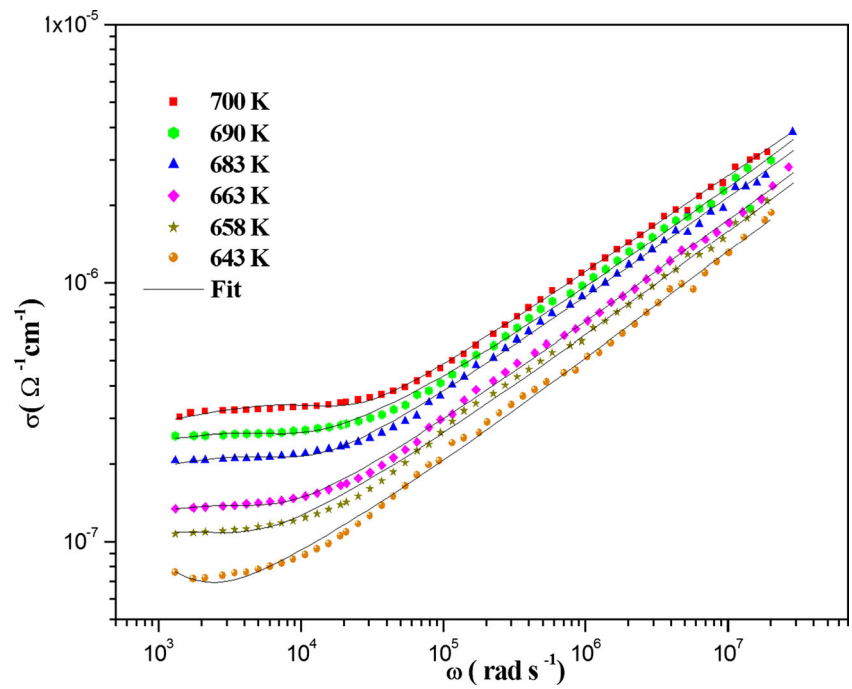
frequency, the hopping takes place by charge carriers through trap sites separated by energy barriers of varied heights. This typical behavior suggests the presence of a hopping mechanism between the allowed sites [38]. The conductivity results are fitted by the following equation referred to as Jonscher's law [39]. Taking into account the fitting procedure, A and n values have been varied simultaneously to get the best fits.

$$\sigma_{AC}(\omega) = \sigma_{DC} + A\omega^n \qquad (9)$$

where σ_{DC} is the DC conductivity, A is a constant temperature-dependent parameter, and n is the power law exponent, where $0 < n < 1$. As a matter of fact, n represents the degree of interaction between mobile ions with the environments surrounding them and A determines the strength of polarizability.

Fig. 9 The exponent factor, n, as a function of temperature of the II-NaFeP$_2$O$_7$ ceramic sample
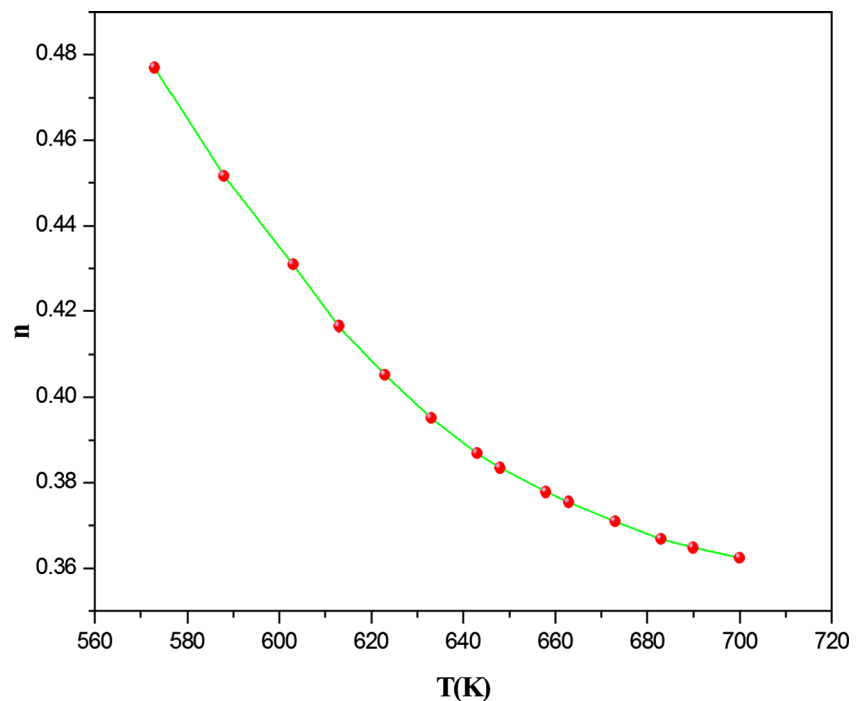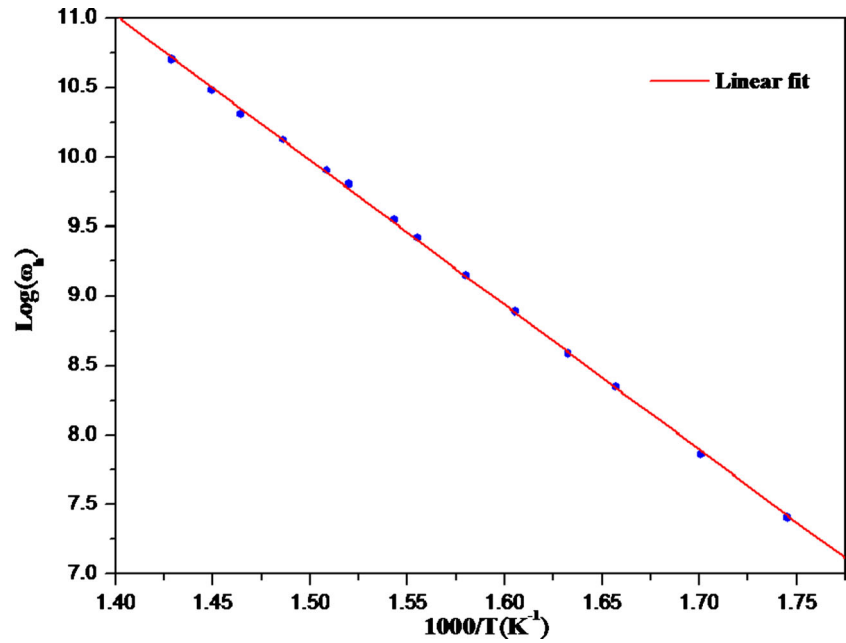
Fig. 10 Temperature dependence of the hopping frequency ω_h

Added to that, the obtained values of (n) for the sample under investigation are in the range of 0.362–0.476, in which the values decrease with the rise in temperature as shown in Fig. 9.

Following, the hopping rate, ω_h has been obtained by using the equation:

$$\omega_h = \left(\frac{\sigma_{DC}}{A}\right)^{1/n} \tag{10}$$

The DC conductivity represents the random process in which the ion diffuses throughout the network by performing repeated hops between charge-compensating sites [40].

Figure 10 depicts the dependence of the hopping frequency, and it follows the Arrhenius behavior. In the present ceramic sample, the hopping frequency and DC conductivity are thermally activated indicating that both are originating from the sodium ion migration. The activation energy extracted from the slope of the plot is 0.85 (3) eV. The near value of

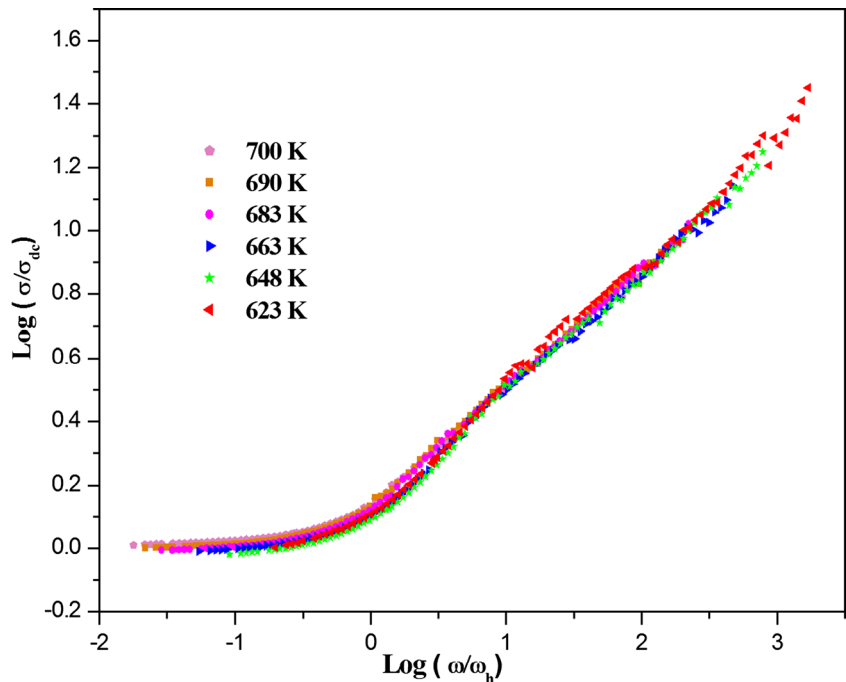**Fig. 11** The scaled conductivity Log (σ_{AC} / σ_{DC}) vs. Log (ω / ω_h)

Table 2 Activation energies and conductivities at 573 K for NaFeP$_2$O7 and AgFeP$_2$O7 compounds

	AgFeP$_2$O$_7$ [13]	NaFeP$_2$O$_7$ [this study]
E_a (±0.03 eV)	0.89	0.84
σ_{573K} (Ω^{-1}cm^{-1})	1.04 10^{-5}	1.11 10^{-6}

activation energies, obtained from the analyses of impedance and conductivity data suggesting the mobility of the charge carrier, is due to a hopping mechanism in the tunnel-type cavities occurring in the structure of the title compound.

In addition, we consider the scaling of the conductivity spectra at different temperatures. In the past few years, different scaling models have been proposed [41, 42]. We have scaled the conductivity spectra by a scaling process [43] reported recently.

To put it simply, the AC conductivity is scaled by σ_{DC}, while the frequency axis is scaled by the crossover frequency ω_h, which is expected to be more appropriate for scaling the conductivity spectra of ionic conductors, since it takes into account the dependence of the conductivity spectra on the structure and the possible changes of the hopping distance experienced by the mobile ions [42]. As shown in Fig. 11, the scaled AC conductivity data collapsed into a single curve and it implies that the relaxation dynamics of charge carriers in the present sample is independent of temperature and compositions [43].

The electrical properties of II-NaFeP$_2$O$_7$ can be compared with those relative to AgFeP$_2$O$_7$. Although they are isostructural, the materials show different features in the conductivity parameters presented in Table 2. In fact, the differences between both compounds are due to the different alkali cation radii : r (Ag$^+$)=1.15 Å and r (Na$^+$)=1.09 Å. As expected, the better activation energy of the title compound can be attributed to a lower Na$^+$ radii with regard to Ag$^+$ ion. Otherwise, it is also related to the wide bottlenecks of the tunnels in NaFeP$_2$O$_7$ (bottlenecks of 4.45 Å). However, the low polarizability of the Na$^+$ ion explains the lower conductivity of the investigated compound.

Conclusions

Overall, this research paper reports the results of a systematic investigation on AC conductivity, AC conductivity scaling, and electrical modulus of II-NaFeP$_2$O$_7$ compound synthesized by the classic ceramic method. X-ray structural analysis exhibits the formation of a single-phase monoclinic at room temperature. Two semicircles are observed in an impedance plot indicating the presence of two relaxation processes in the compound associated with grain and grain boundary. Indeed, the dielectric data have also been analyzed in modulus formalism. Similarly, two dielectric relaxation peaks thermally activated in the modulus loss spectra confirmed the grain and grain boundary contribution to electrical response in the title compound. Also, AC conductivity measurements and its scaling analysis are studied on the II-NaFeP$_2$O$_7$ in the frequency range from 209 Hz to 5 MHz and in the temperature range from 573 to 700 K. Finally, the activation energies obtained from the impedance and modulus spectra are proven to be close, suggesting that the ionic transport in the investigated material can be described by a hopping mechanism.

References

1. Kim JS, Lee KH, Cheon CI (2009) J Electroceram 22:233–237
2. Kim JW, Yoon DC, Jeon MS, Kang DW, Kim JW, Lee HS (2010) Curr Appl Phys 10:1297–1301
3. Jacob J, Abdul Khadar M, Lonappan A, Mathew KT (2008) Bull Mater Sci 31:847–851
4. Ben Rhaiem A, Chouaib S, Guidara K (2010) Ionics 16:455–463
5. Zhang G, Jiang S, Zhang Y, Xie T (2009) Curr Appl Phys 9:1434–1437
6. Kim H, Shakoor RA, Park C, Lim SY, Kim J-S, Jo YN, Cho W, Miyasaka K, Kahraman R, Jung Y, Choi JW (2013) Adv Funct Mater 23:1147–1155
7. Uebou Y, Okada S, Egashira M, Yamaki J-I (2002) Solid State Ionics 148:323
8. Barpanda P, Nishimura S-I, Yamada A (2012) Adv Energy Mater 2:841
9. Ordoñez Regil E, García González N, BarocioAm SM (2012) J Anal Chem 3:512
10. Parajón-Costa BS, Mercader RC, Baran EJ (2013) J Phys Chem Solids 74:354–359
11. Gamondes JP, d'Yvoire F, Boulle A (1971) CR Acad Sci Paris 272:49
12. Grunze I, Grunze H, Anorg Z (1984) Allg Chem 512:39
13. Moya-Pizarro T, Salmon R, Fournes SL, Le Flem G, Wanklin BS, Hagenmuller P (1984) J Solid State Chem 53:387
14. Nasri S, Megdiche M, Guidara K, Gargouri M (2013) Ionics 19:1921–1931
15. Nasri S, Megdiche M, Gargouri M, Guidara K. doi: 10.1007/s11581-013-0969-z
16. Gabelica Robert M, Goreaud M, Ph L, Raveau B (1982) J Solid State Chem 45:389–395
17. Terebilenko KV, Kirichok AA, Baumer VN, Maksym S, Slobodyanik NS, Gütlich P (2010) J Solid State Chem 183:1473–1476
18. Yakuphanoglu F, Yahia IS, Barim G, Filiz Senkal B (2010) Synth Met 160:1718
19. Macdonald JR (1987) Impedance spectroscopy. Wiley, NY
20. Kumar P, Singh BP, Sinha TP, Singh NK (2011) Physica B 406:139–143
21. Ang C, Yu Z, Jing Z, Lunkenheimer P, Loidl A (2000) Phys Rev B 61:3922–3926
22. Bauerle JE (1969) J Phys Chem Solids 30:2657
23. Cole KS, Cole RH (1941) J Chem Phys 9:341
24. Mahamoud H, Louati B, Hlel F, Guidara K (2011) J Alloys Compd 509:6083–6089

25. Megdiche M, Perrin-pellegrino C, Gargouri M (2014) J Alloys Compd 584:209–215
26. Kumar A, Manna I (2008) Physica B 403:2298–2305
27. Borsa F, Torgeson DR, Martin SW, Patel HK (1992) Phys Rev B 46: 795
28. Mahato DK, Dutta A, Sinha TP (2011) Indian J Pure Appl Phys 49: 613–618
29. Nagi KL, Leon C (1998) Solid State Ionics 125:81
30. Pissis P, Kyritsis A (1997) Solid State Ionics 97:105
31. Oueslati A, Hlel F, Guidara K, Gargouri M (2010) J Alloys Compd 492:508–514
32. Saha S, Sinha TP (2002) Phys Rev B65:134103–134107
33. Padmasree KP, Kanchan DK, Kkulkarni AR (2006) Solid State Ionics 177:475–482
34. Louati B, Guidara K, Gargouri M (2009) J Alloys Compd 472:347–351
35. Rao KS et al (2008) J Alloys Compd 464:497–507
36. Mahato DK, Alo D, Sinha TP (2011) Physica B 406:2703–2708
37. Saha S, Sinha TP (2002) Phys Rev B 65:134103–134107
38. Behera B et al (2007) J Alloys Compd 436:226–232
39. Jonscher AK (1977) Nature 267:673
40. Louati B, Gargouri M, Guidara K, Mhiri T (2005) Phys Chem Solids 66:762
41. Roling B, Happe A, Funke K, Ingram MD (1997) Phys Rev Lett 78: 2160
42. Ghosh A, Pan A (2000) Phys Rev Lett 84:2188
43. Pan A, Ghosh A (2002) Phys Rev B 66:012301